Force-induced on-rate switching and modulation by mutations in gain-of-function von Willebrand diseases

Jongseong Kim[1], **Nathan E. Hudson**[1], **and Timothy A. Springer**[2]

Program in Cellular and Molecular Medicine, Children's Hospital Boston, Boston, MA 02115; and Department of Biological Chemistry and Molecular Pharmacology, Harvard Medical School, Boston, MA 02115

Contributed by Timothy A. Springer, January 26, 2015 (sent for review October 17, 2014; reviewed by Shaun Jackson and J. Evan Sadler)

Mutations in the ultralong vascular protein von Willebrand factor (VWF) cause the common human bleeding disorder, von Willebrand disease (VWD). The A1 domain in VWF binds to glycoprotein Ibα (GPIbα) on platelets, in a reaction triggered, in part, by alterations in flow during bleeding. Gain-of-function mutations in A1 and GPIbα in VWD suggest conformational regulation. We report that force application switches A1 and/or GPIbα to a second state with faster on-rate, providing a mechanism for activating VWF binding to platelets. Switching occurs near 10 pN, a force that also induces a state of the receptor–ligand complex with slower off-rate. Force greatly increases the effects of VWD mutations, explaining pathophysiology. Conversion of single molecule k_{on} (s^{-1}) to bulk phase k_{on} ($s^{-1}M^{-1}$) and the k_{on} and k_{off} values extrapolated to zero force for the low-force pathways show remarkably good agreement with bulk-phase measurements.

Understanding how force affects receptor and ligand binding and unbinding is a long-standing effort in mechanobiology (1–5). Bond dissociation rates typically increase under mechanical stress; however, bond stability can be enhanced through specialized mechanisms induced by force, including catch bonds and switching to a slip bond with a slower off-rate (flex bonds) (6, 7). Bond formation against an applied force has recently been measured (8). Force-regulated switching to a faster on-rate has not yet been reported for any receptor–ligand bond but would have important biological implications for adhesion in environments with high forces such as the circulation.

At sites of vascular injury, hydrodynamic force in the bloodstream acting on von Willebrand factor (VWF) is pivotal in regulating the binding of the VWF A1 domain to GPIbα on platelets and commencing the crosslinking of platelets by VWF to form a platelet plug (9–11). VWF circulates in the form of long, disulfide-bonded concatemers, with tens to hundreds of monomers, which mostly adopt a compact, irregularly coiled conformation during normal hemodynamics (12). At sites of hemorrhage, flow changes from shear to elongational. On transition from low to high shear and from shear to elongational flow, irregularly coiled molecules extend to a thread-like shape, and elongational (tensile) force is exerted throughout their lengths (13–16). Molecular elongation exposes the multiple A1 binding sites in VWF concatamers for multivalent binding to GPIbα (9, 11, 14, 16–18).

In vivo, tensile force transmitted through VWF is applied to the N and C termini of individual domains, and could theoretically change A1 domain conformation before binding to GPIbα. Although this scenario has not yet been observed, single-molecule studies demonstrate two distinct force-dependent dissociation pathways (flex-bond behavior) of the wild-type (WT) A1-GPIbα complex, and thus suggest that two conformational states can be present after formation of the receptor–ligand complex (6).

Mutations in VWF cause von Willebrand disease (VWD), the most common human heritable bleeding disorder (11, 17). In type 2B VWD, gain-of-function mutations localized to the A1 domain enhance binding to GPIbα. These mutations map distal to the GPIbα binding site, near the A1 N and C termini where elongational force is applied to VWF during physiologic activation (19–21). Gain-of-function mutations in GPIbα cause a disease similar to type 2B VWD termed platelet-type VWD (PT-VWD) (22). PT-VWD mutations map to a β-switch region that changes conformation when complexed with A1 to form a β-ribbon structure in GPIbα that adds onto the β-sheet in A1 (20, 21, 23). PT-VWD mutations are thought to favor the conformation that the β-switch assumes when bound to A1, and map adjacent to the major A1-GPIbα interface. Here, using single molecule measurements, we show that the formation of the A1-GPIbα bond is allosterically regulated by force-dependent switching between two distinct association pathways, suggesting two different conformational states before binding. Pathologic gain-of-function mutations retained two-state binding and unbinding and showed faster on-rates together with slower off-rates under force than WT. A1 and GPIbα mutations showed distinct effects on kinetic and mechanical properties.

Results

We used receptor and ligand in a single molecule (ReaLiSM) constructs of A1-GPIbα with or without the VWD R1306Q mutation in VWF A1 or the PT-VWD M239V mutation in GPIbα (Fig. 1*A*). Receptor–ligand unbinding and rebinding gave discrete jumps in tether length in each cycle of stretch and relaxation, respectively (Fig. 1*B*). Fits to the worm-like chain model (WLC) (24) for ReaLiSM constructs with 26- and 43-residue linkers gave contour lengths of 12.1 ± 0.9 nm and 17.7 ± 0.6 nm (Fig. 1*C*) in agreement with calculated values of 11.4 nm and 17.9 nm, respectively, based on 3.8 Å per linker residue and N- to C-terminal distances of 1.9 nm (A1), 7 nm (GPIbα), and 7 nm (A1-GPIbα complex) from crystal structures (20, 23). This agreement, together with B to S transitions of the DNA handles at ~67 pN (24) observed in all of our experiments (*Materials and Methods*), provided

Significance

Binding of von Willebrand factor (VWF) to platelets is regulated by hydrodynamic forces in the vasculature. VWF can sense force and can bind when the hydrodynamics change due to bleeding. We show that force application switches the A1 domain in VWF to a second state with faster on-rate for its binding partner on platelets, GPIbα. This provides a physiological mechanism for activating VWF binding to platelets at sites of bleeding. Moreover, force increases the effects of gain-of-function mutations found in von Willebrand disease (VWD) and platelet-type VWD by mechanically stabilizing bond formation and strength.

Author contributions: T.A.S. designed research; J.K., N.E.H., and T.A.S. performed research; J.K., N.E.H., and T.A.S. analyzed data; and J.K., N.E.H., and T.A.S. wrote the paper.

Reviewers: S.J., Monash University; and J.E.S., Washington University School of Medicine.

The authors declare no conflict of interest.

[1] J.K. and N.E.H. contributed equally to this work.

[2] To whom correspondence should be addressed. Email: Timothy.Springer@childrens.harvard.edu.

This article contains supporting information online at www.pnas.org/lookup/suppl/doi:10.1073/pnas.1501689112/-/DCSupplemental.

www.pnas.org/cgi/doi/10.1073/pnas.1501689112

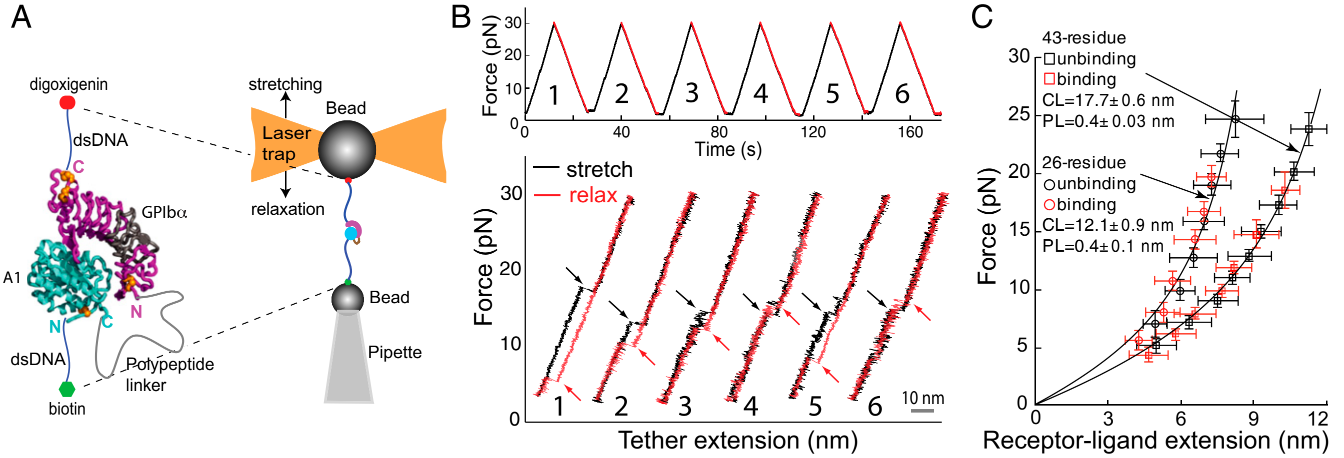

Fig. 1. The VWF A1 and GP1bα ReaLiSM construct and change in extension upon unbinding and rebinding. (*A*) Schematic of the ReaLiSM construct and tweezers (6). (*B*) Successive cycles of stretching (black traces) and relaxation (red traces) with unbinding and rebinding events arrowed, with the R1306Q construct at 40 nm/s. (*C*) Fits to worm-like chain model showing the persistence length (PL) and contour length (CL). Bars show SD for each force bin.

strong support that single A1-GPIbα binding and unbinding events were being measured.

The distribution of bond dissociation forces for A1/R1306Q-GPIbα/WT and A1/WT-GPIbα/M239V was bimodal (Fig. 2 *D*–*I*), as previously reported for WT (6) (Fig. 2 *A*–*C*). Thus, all three types of complexes behave as flex bonds, switching from one state at low force to a second state at higher force. However, the mutations shifted the rupture force distributions. The second peak at higher force at a pulling rate of 40 nm/s shifted from WT value of 14.6 pN to 18.0 pN in GPIbα/M239V (Fig. 2 *B* and *E*) and to 21.6 pN in A1/R1306Q (Fig. 2*H*).

Bond lifetimes at each force bin in rupture force histograms were estimated using the Dudko–Hummer–Szabo equation (25). Data at two different pulling rates and linker lengths demonstrated excellent agreement with no adjustable parameters (Fig. 2 *J*–*L*). Off-rates for dissociation pathways at low force ($k_{1\ \mathrm{off}}$) and high force ($k_{2\ \mathrm{off}}$) were each well fit by the Bell model, $k_{\mathrm{off}} = k^0_{\mathrm{off}}$ exp $(\sigma F/k_BT)$, where the force across the receptor–ligand bond exponentially increases off-rate. WT results (Fig. 2*J*) were within error of previous estimates (6). Interestingly, the mutations had significantly different effects on the extrapolated off-rate at zero force, k^0_{off}, and the mechanical stability of the bond, σ, which is equivalent to the distance to the transition state and determines how much force exponentiates k_{off}. The $k_1{}^0_{\mathrm{off}}$ and $k_2{}^0_{\mathrm{off}}$ values for wild-type and A1 mutant were comparable, whereas those of the GPIbα mutant were about twofold and fourfold slower, respectively. Conversely, the A1 mutation increased bond strength (decreased σ_1 and σ_2 values) more than the GPIbα mutation (Fig. 2 *K* and *L*).

Association kinetics were investigated by observing rebinding forces (Figs. 1*B* and 3). Interestingly, we saw bimodal rebinding histograms for all three types of A1-GPIbα complexes (Fig. 3). Compared with WT (Fig. 3 *A*–*C*), the two peaks were more separated for patient mutations and were shifted to higher force (Fig. 3 *D*–*I*). The presence of two peaks in rebinding force demonstrates that before binding, either A1, GPIbα, or both can exist in two different states that differ in binding kinetics. Binding histograms for the PT-VWD mutation showed a shift in both peaks compared with WT; the first pathway shifted from 4.7 pN to 8.8 pN, and the second shifted from 9.3 pN to 15.6 pN at 40 nm/s (Fig. 3 *B* and *E*). In the VWD type 2B mutation, the first pathway shifted from 4.7 pN to 6.7 pN, and the second rupture force peak was shifted from 9.3 pN to 12.6 pN at 40 nm/s (Fig. 3*H*). Bimodal binding force histograms were further observed in the constructs with a shorter linker (Fig. 3 *C*, *F*, and *I*).

Dissociation and reassociation through low-force and high-force pathways were observed in successive cycles with the same tether (Fig. 1*B*). We compared the frequency of successive events to that expected based on overall frequency at each pulling rate (Table S1). There was no evidence of hysteresis; e.g., the frequency of unbinding or rebinding at high force was independent of whether the previous event was at high force. This suggests that state switching occurred more rapidly than the half-cycle time of 12 s at 40 nm/s (Fig. 1*B*) or 24 s at 20 nm/s. In agreement, state-switching rates for bond dissociation were previously estimated to be in the range of 0.13–1.17 s^{-1} at 10–11 pN (6).

Expressions have recently been derived for extracting single-molecule on-rates from distributions of binding forces at different relaxation speeds for a receptor–tether–ligand (RTL) complex (Fig. 3 *J*–*L*) (26). The effects of the 43- and 26-residue tethers can be accounted for and removed using the worm-like chain parameters measured in Fig. 1*C*, revealing true receptor–ligand (RL) binding parameters (26) (See *SI Materials and Methods* and Figs. S1 and S2). Fitting and converting to RL values yields three distinct parameters: $k^{0\ \mathrm{RL}}_{\mathrm{on}}$, the zero-force on-rate corresponding to the intrinsic, unimolecular on-rate measured in s^{-1} (1); $\sigma^{\mathrm{RL}}_{\mathrm{on}}$, the mechanical sensitivity of on-rate to force; and ΔG^{RL}, the height of the energy barrier to rebinding (Tables S2 and S3). Average RL parameters derived from measurements with the 43- and 26-residue linkers are shown in Fig. 3*M*. For WT and both mutants, $k_2{}^{0\ \mathrm{RL}}_{\mathrm{on}}$ was 11- to 17-fold faster than $k_1{}^{0\ \mathrm{RL}}_{\mathrm{on}}$, showing a large difference between the two association pathways. Within each pathway, on-rates for WT, A1 R1306Q, and GPIbα M239V were comparable, with differences of less than 1.2-fold. The most dramatic difference between WT and mutant behavior manifested in the exponential σ values, which govern the force dependence of on-rates; σ_1 decreases from 2.5 nm in WT to 1.4 nm and 1.5 nm, and σ_2 decreases from 1.8 nm in WT to 1.0 nm and 1.1 nm for M239V and R1306Q, respectively. Thus, gain of function A1 R1306Q and GPIbα M239V mutations mechanically stabilize bond formation.

Discussion

We have demonstrated that force can switch the states of VWF A1 and/or GPIbα, resulting in two distinct receptor–ligand association pathways. Our finding that force can switch the kinetics of bond formation between A1 and GPIbα is unprecedented for a RL bond. Usually, receptors and ligands have no significant forces exerted on them before binding; it is only after binding that force on cell(s) is applied to the RL bond. Thus, previous theories on how catch or flex bonds work have focused on the RL complex and only considered the effect on bond dissociation (6, 7). Because integrin–ligand and selectin–ligand complexes

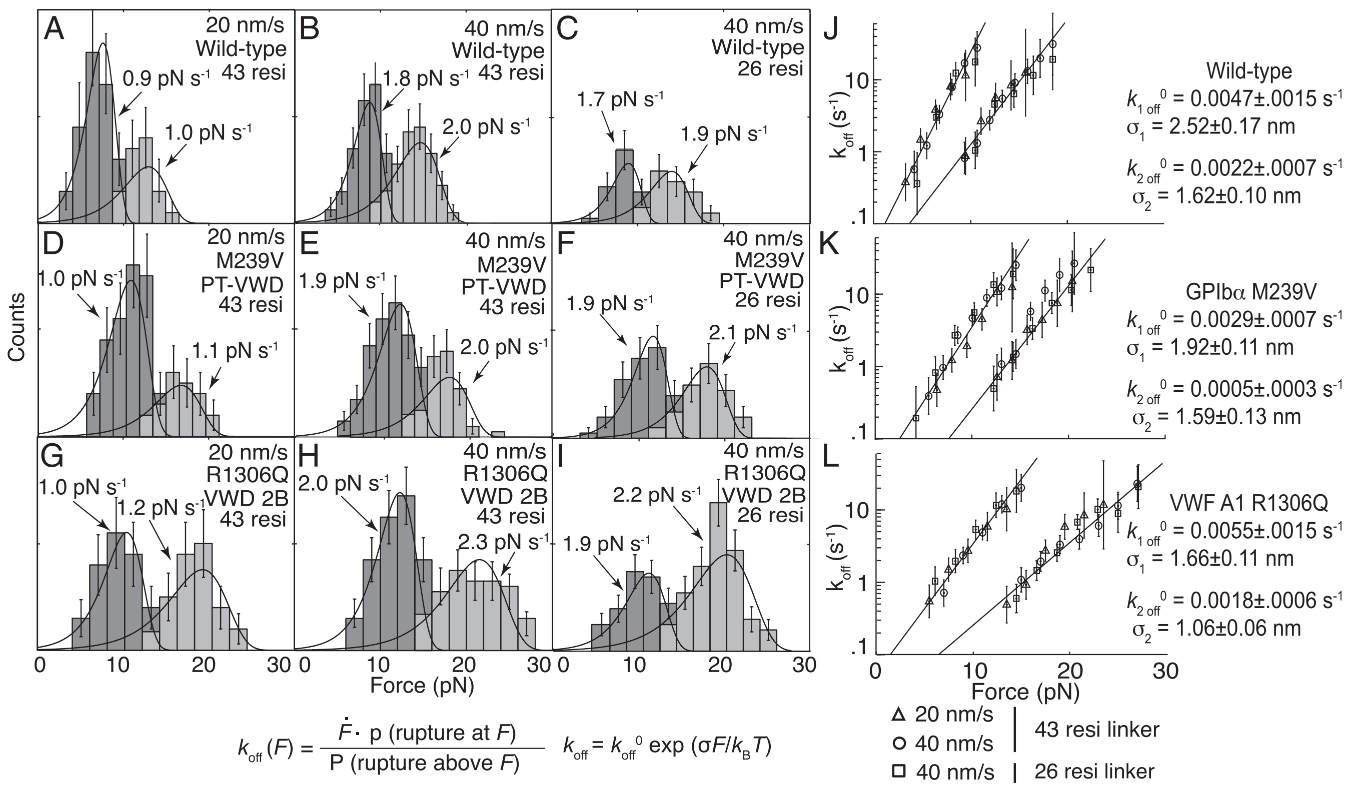

$$k_{\mathrm{off}}(F) = \frac{\dot{F} \cdot \text{p (rupture at } F)}{\text{P (rupture above } F)} \qquad k_{\mathrm{off}} = k_{\mathrm{off}}^{0} \exp(\sigma F / k_B T)$$

Fig. 2. Force spectroscopic measurements of k_{off}. (*A–I*) Unbinding force distributions at different pulling rates in wild-type (*A–C*), M239V (*D–F*), and R1306Q (*G–I*) constructs. Error bars show the variance, estimated assuming a binomial distribution for each histogram bin, with the square of variance = $n(1\text{-}n/N_c)$, where n is events in a particular bin and N_c is total events (35). Curves show the predicted rupture force distributions using the constants from *J–L* for dissociation pathways 1 (left curve, estimated using dark gray histogram bins) and 2 (right curve, estimated using light gray histogram bins). Events in the overlap region were apportioned between the pathways according to iterative fits. Counts are on a linear scale with maximal values of 20 for *A*, *D*, and *G*; 40 for *B* and *C*, *E* and *F*, and *H* and *I*. (*J–L*) The k_{off} (F) values (where F is Force) calculated for each bin in *A–I* are plotted. Lines and constants in each panel are from fits of k_{off} (F) to k_{off}^{0} and σ. Error bars show 1 SD.

are more extended in their high- than low-affinity states, one theory posits that by favoring extension, the applied force lowers the energy of the high-affinity relative to the low-affinity state (4).

VWF is an exceptional ligand. The length of VWF concatamers (Fig. 4*A*) can exceed the diameter of cells and the elongational forces applied to free VWF in the bloodstream range up to 10 pN, similar to the force range studied here (16). When bound to platelets on the vessel wall, the force on VWF would be much greater (14). In the irregularly coiled conformation of VWF concatemers at low flow, A1 may interact with other domains. However, elevated shear and elongational flows found at sites of hemostasis will tend to induce a thread-like, uncoiled conformation of VWF (Fig. 4*B*) (14). By definition, elongation removes interactions with distal domains in the same or other monomers within a VWF concatemer. Notably, A1 also contains mucin-like N- and C-terminal segments (Fig. 4*A*) that act as spacers to separate it from neighboring domains (14) after elongation. In elongated VWF, force is applied to the N and C termini of A1 (Fig. 4 *B* and *D*) and propagates through A1 similarly to A1 in the unbound state of ReaLiSM (Fig. 4*E*). In contrast, no significant force would be applied to GPIbα on the surface of a platelet before binding A1. Because of these physiologic considerations, and the proximity of VWD type 2B mutations to the site of force application to A1 (Fig. 4 *C* and *D*), it is reasonable to suggest that the two on-rates may correspond to two distinct conformations of A1, but this remains to be formally demonstrated.

It is interesting to convert our intrinsic single molecule $k_{\mathrm{on}}^{0\ \mathrm{RL}}$ rate estimates in units of s^{-1} to bulk k_{on} rates ($k_{\mathrm{on}}^{\mathrm{sol}}$) in units of $\mathrm{M}^{-1}\mathrm{s}^{-1}$ using a model for effective concentration in an encounter complex (Fig. 4*F*). The encounter complex is formed when two reactants diffuse sufficiently close to one another for the subsequent binding reaction to occur (27, 28). The distance between the two reactants in the encounter complex is used to calculate the concentration at which the intrinsic on-rate in s^{-1} occurs, and thus to convert to the bulk rate on-rate in $\mathrm{M}^{-1}\mathrm{s}^{-1}$. In our model of the encounter complex, we have assumed that σ_{on} and σ_{off} correspond to distances to transition states between unbound and bound states, respectively, and added these distances to the distance between the centers of masses of A1 and GPIbα in complex crystal structures (Fig. 4*F*). The $k_{1\ \mathrm{on}}^{\ \mathrm{sol}}$, $k_{1\ \mathrm{off}}^{\ 0}$, and 3D dissociation constants ($K_D = k_{1\ \mathrm{off}}^{\ 0}/k_{1\ \mathrm{on}}^{\ \mathrm{sol}}$) calculated from our measurements on WT, VWD type 2B, and PT-VWD ReaLiSM constructs match remarkably well with bulk-phase values from two well-documented reports (21, 29) (Fig. 4*G*). These agreements provide an important confirmation of the ability of the ReaLiSM construct to measure meaningful force-induced binding kinetics.

Off-rates have been estimated by other studies that report either single molecule or single tether A1-GPIbα measurements. Using thermal fluctuation of beads coated with A1 and antibody bound to GPIbα, a zero-force off-rate of 0.2 s^{-1} was found (30). Transient tethers of A1-coated beads in shear flow over surfaces coated with platelets were extrapolated to zero force using the Bell model and yielded k_{off}^{0} of 3 s^{-1} and σ of 0.03 nm (31). These off-rates differ by two to three orders of magnitude from our $k_{1\ \mathrm{off}}$ measurement of 0.0047 s^{-1} and the bulk phase measurement of 0.0036 s^{-1} (29). The σ value of 0.03 nm (31) also differs greatly from our estimate of 2.5 nm. These discrepancies suggest that

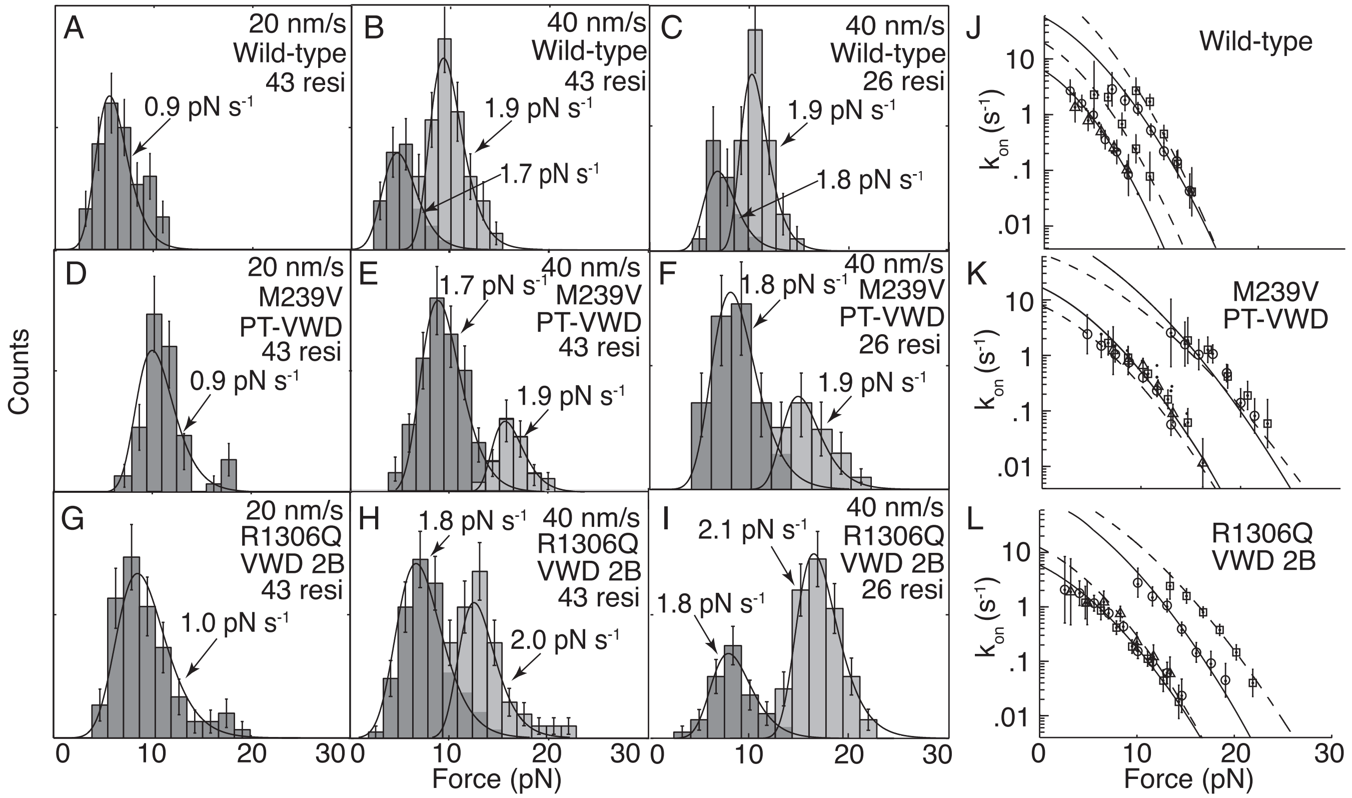

$$k_{on}(F)=\frac{\dot{F}*P(\text{binding at }F)}{P(\text{binding below }F)}$$

$$p(F)=\frac{k_{on}(F)}{|\dot{F}(F)|}\exp\left[-\frac{k_BT*k_{on}(F)}{|\dot{F}(F)|*\sigma_{on}{}^{RTL}}\left(1+\frac{\kappa_s}{\kappa_u(F)}\right)^{\frac{v}{v-1}}\left(1+\frac{vF\sigma_{on}{}^{RTL}}{\Delta G_{on}{}^{RTL}}\right)^{1-\frac{1}{v}}\right]$$

M

	State 1			State 2		
	$k_{1\,on}^{0\,RL}$ (s^{-1})	$\sigma_{1\,on}^{RL}$ (nm)	ΔG^{RL} (k_BT)	$k_{2\,on}^{0\,RL}$ (s^{-1})	$\sigma_{2\,on}^{RL}$ (nm)	ΔG^{RL} (k_BT)
Wild-type	3.4±1.9	2.5±0.5	2.9±0.7	40±16	1.8±0.2	2.1±0.4
M239V PT-VWD	3.9±1.6	1.4±0.2	2.0±0.4	44±17	1.0±0.1	1.8±0.3
R1306Q VWD 2B	3.1±1.5	1.5±0.3	2.0±0.5	54±17	1.1±0.1	1.7±0.3

△ 20 nm/s | 43 resi linker ——
○ 40 nm/s
□ 40 nm/s | 26 resi linker - - - -

Fig. 3. Force spectroscopic measurements of k_{on}. (*A–I*) Binding force distributions at different relaxation rates for wild-type (*A–C*), M239V (*D–F*), and R1306Q (*G–I*) constructs. Errors are variance, estimated as in Fig. 2. Histograms were fit to the Pierse–Dudko equation (bottom equation) (26) using least-squares (*SI Materials and Methods*) yielding the probability distributions for rebinding pathways 1 (left curve, dark gray bins) and 2 (right curve, light gray bins). Events in the overlap region (histogram bins with dark and light gray) were apportioned between the pathways according to iterative fits. Force relaxation rates (PN/s) were averaged over bins for each pathway and are shown in each panel. Counts are on a linear scale with maximal values of 20 for *C* and *F*, 30 for *A*, *B*, *D*, and *G*, and 40 for *E* and *H–I*. (*J–L*) The k_{on}(F) values (where F is force) calculated from each bin in *A–I* are plotted. Error bars show SD. (*M*) Force-dependent A1-GPIbα RL binding constants, calculated after removal of the effect of the tether (26) (*SI Materials and Methods*). Data are average RL values from experiments using 43- and 26-residue linkers ±1 SD estimated by propagation of error.

bead thermal motion and transient tethers measure different types of events than binding and unbinding of single A1 and GPIbα molecules measured with ReaLiSM or bulk studies.

We found that force greatly increases the effect of VWD mutations. At zero force in state 1, the VWD type 2B R1306Q A1 and PT-VWD M239V GPIbα mutations enhance bond formation and bond lifetime values by less than 1.2-fold (Fig. 4*G*). These are modest changes considering the resulting disease phenotype but not too dissimilar from bulk measurements that show twofold to fivefold increases in affinity (Fig. 4*G*) (20, 21, 29). In contrast, large differences in kinetics are observed once force is applied. At 15 pN in state 2, bond formation occurs ~45-fold faster than WT for both VWD 2B and PT-VWD mutants (Fig. 4*G* and Table S4). Bond dissociation by the mutants is also slower than WT at 15 pN in state 2, so the VWD 2B and PT-VWD mutations have an effective 260-fold and 230-fold increase in affinity, respectively (Fig. 4*G*). Therefore, an important concept emerging from these results is that force can accentuate the manifestation of disease phenotypes. In VWD 2B and PT-VWD, enhanced binding of VWF to platelets leads to depletion of VWF, with longer concatemers selectively depleted, and also to depletion of platelets; the final result is bleeding tendency (11, 17).

Our finding of force-induced switching to a faster on-rate extends the concept of flex bonds from bond dissociation to bond association. For WT, VWD-2B, and PT-VWD, switching to a state with faster on-rate resulted in a 40- to 100-fold increase in bond

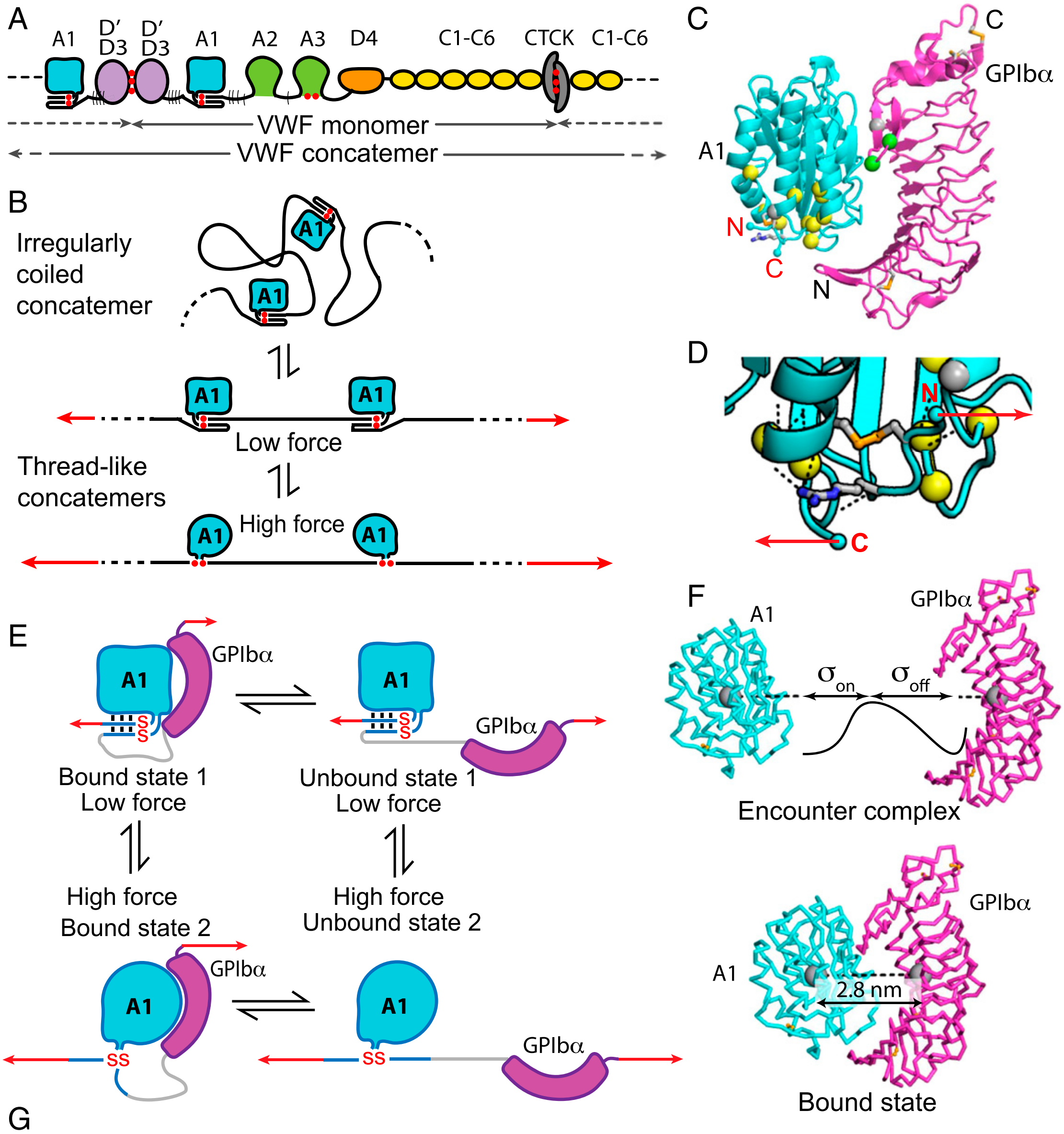

G

	Wild-Type			PT-VWD (M239V)			VWD type 2B (R1306Q)		
	k_{off} (s^{-1}x10^{-3})	k_{on} ($M^{-1}s^{-1}$x10^{-3})	K_D (μM)	k_{off} (s^{-1}x10^{-3})	k_{on} ($M^{-1}s^{-1}$x10^{-3})	K_D (μM)	k_{off} (s^{-1}x10^{-3})	k_{on} ($M^{-1}s^{-1}$x10^{-3})	K_D (μM)
Bulk, Blenner et al.			2.5±0.7						1.0±0.2
Bulk, Miura et al.	3.6±0.2	1.1±0.1	3.3±0.5	3.2±0.8	4.7±1.3	0.63±0.1			
SM, (0 pN, k_1)	4.7±1.5	4.1±2.3	1.1±0.7	2.9±0.7	2.3±0.9	1.3±0.6	5.5±1.5	1.7±0.8	3.3±1.8
SM, (15 pN, k_2)	810±390	0.15±0.08	(5.2±3.7)x10^3	160±130	7.0±2.8	23±21	86±34	4.2±.1.3	20±10

Fig. 4. Models for force-dependent activation of VWF and comparison of single-molecule and bulk measurements. (*A*) Schematic organization of domains in VWF and head-to-head and tail-to-tail linkage of VWF monomers into concatemers. (*B*) VWF concatemers in low shear are predominantly irregularly coiled; transition to high shear and elongational flow induces a thread-like conformation. High tensile force exerted through concatemers is hypothesized to cause a change in A1 conformation similar to that in the ReaLiSM construct shown in *E*. (*C*) Crystal structure of A1 bound to GPIbα (21). Cα spheres show sites of VWD type 2B mutations in A1 (36) (yellow, except R1306 in silver) and PT-VWD mutations in GPIbα (37) (yellow, except M239 in silver). (*D*) Enlargement of the region near the A1 N and C termini. Hydrogen bonds (black dashes) external to the long-range disulfide (sulfur atoms shown in orange) would be broken by force applied (red arrows) to the N and C termini (small cyan spheres) before the disulfide bond would resist force. Breakage of these hydrogen bonds might trigger conversion of A1 to a high-affinity state (14), as shown schematically in *B* and *E*. (*E*) Model of force-dependent switching between two conformational states consistent with the two pathways for force-dependent unbinding and binding measured here. Red arrows in *B*, *D*, and *E* represent tensile force. (*F*) Single-molecule encounter complex model. To convert to bulk-phase on-rate units, the effective concentration of one reactant relative to the other is determined as the volume of a sphere of radius equal to the separation between the center of mass of A1 and GPIbα in the bound state (*Lower*) plus σ_{on} and σ_{off} (*Upper*). (*G*) Comparison between bulk-phase kinetic and K_D values from Blenner et al. (21) and Miura et al. (29) and our single-molecule (SM) data with k_{on} converted to bulk-phase units. Values at 0 pN in state 1 are for comparison with bulk-phase values. Values at 15 pN in state 2 enable comparison between wild-type and mutants in a physiologically relevant force range.

association kinetics at 15 pN. Force-induced switching may therefore dramatically enhance bond formation under flow. The hypothesis that a similar conformational change underlies second states of both bond dissociation and association will be an important subject for future structural studies. Switching to each of these second states occurs at ∼10 pN; furthermore, the GPIbα cytoplasmic domain remains bound to filamin at forces in this region (32) and, together with the covalently linked GPIbβ subunits (33), helps prevent uprooting from the cell.

At sites of hemostasis and stenosis, alterations in flow are predicted to elongate VWF and increase tensile force exerted throughout its length (14). A1 thus becomes better exposed for binding to platelets; furthermore, our results provide a mechanism for switching A1 to a second state with faster on-rate for GPIbα. In agreement, shear thresholds have been observed, above which, VWF agglutinates platelets in flow and VWF adsorbed to a vessel wall mediates binding and rolling of platelets (9, 10, 34). Thus, the forces unleashed in hemorrhage can trigger binding of VWF to platelets and formation of a hemostatic plug. Moreover, the second state of the A1-GPIbα complex and its greater mechanical strength than state 1 enable resistance to the unusually high forces that must be overcome by a biological RL bond for hemostatic plug formation and final closure of a bleeding vessel.

Materials and Methods

Proteins were expressed and purified as previously described (6). The ReaLiSM construct consists of human VWF A1 domain (Asp-1261 to Pro-1466 with prepro-VWF numbering) and human platelet GPIbα (His-1 to Arg-290) connected by linkers of 26 residues, GTGENLYFQGGSSSSTTGWTGGHVGT; or 43 residues, GTGENLYFQGHHHHHH(GSSSS)$_3$GTTGWRGGHVGT. Our current 43-residue linker lacks the Pro residues present in our previous 43-residue linker (6). Protein was made with or without mutations M239V in GPIbα or R1306Q in A1.

DNA handles (802 bp), protein−DNA coupling, anti-digoxygenin Fab, and streptavidin beads were as previously described (6).

We performed force rip experiments (constant trap velocity) by stretching and relaxing the tether between force values of 2 pN and 15–30 pN at pulling rates of either 20 nm/s or 40 nm/s. The unbinding distance was measured between two points on the force trap position curves, from the point just before the dissociation to the point when the force returned to the same level after dissociation. The extension between these two points arises solely from stretching the flexible polypeptide tether. Force loading rates (pN/s) before each rip event were estimated from the curve by measuring the slope of the force vs time data; this value was then averaged over all events in a given histogram bin of unbinding events at a given pulling speed.

Rebinding was observed in force rip experiments as force was lowered during the relaxation phase of the cycle. We define the rebinding force as the highest force at which rebinding was observed in one relaxation cycle. Most cycles only showed one unbinding and one rebinding event; however, hopping between bound and unbound states in one cycle was not uncommon for the R1306Q construct, as shown in Fig. 1*B*. Binding events were binned as a function of force.

Equations, fitting methods, and estimations required to convert RTL values to RL k_{on}, σ, and ΔG values are described in *SI Materials and Methods*. Briefly, off-rate fitting was performed as described (6). On-rate fitting was performed by minimizing the sum of squared errors between the normalized binding histogram data and the probability of binding function described in ref. 26 using the fminsearch tool in MATLAB. Error bars and errors shown in figures and tables show SD estimated by propagation of error (35).

ACKNOWLEDGMENTS. We are extremely grateful to Olga Dudko, Christopher Pierse, Cheng-Zhong Zhang, Darren Yang, and Wesley Wong for insightful discussions on physical models and calculations. The research was supported by National Institutes of Health Grant HL-108248.

1. Bell GI (1978) Models for the specific adhesion of cells to cells. *Science* 200(4342): 618–627.
2. Lawrence MB, Springer TA (1991) Leukocytes roll on a selectin at physiologic flow rates: Distinction from and prerequisite for adhesion through integrins. *Cell* 65(5): 859–873.
3. Evans EA, Calderwood DA (2007) Forces and bond dynamics in cell adhesion. *Science* 316(5828):1148–1153.
4. Springer TA (2009) Structural basis for selectin mechanochemistry. *Proc Natl Acad Sci USA* 106(1):91–96.
5. Wang X, Ha T (2013) Defining single molecular forces required to activate integrin and notch signaling. *Science* 340(6135):991–994.
6. Kim J, Zhang CZ, Zhang X, Springer TA (2010) A mechanically stabilized receptor-ligand flex-bond important in the vasculature. *Nature* 466(7309):992–995.
7. Evans E, Leung A, Heinrich V, Zhu C (2004) Mechanical switching and coupling between two dissociation pathways in a P-selectin adhesion bond. *Proc Natl Acad Sci USA* 101(31):11281–11286.
8. Rognoni L, Stigler J, Pelz B, Ylänne J, Rief M (2012) Dynamic force sensing of filamin revealed in single-molecule experiments. *Proc Natl Acad Sci USA* 109(48): 19679–19684.
9. Ruggeri ZM, Orje JN, Habermann R, Federici AB, Reininger AJ (2006) Activation-independent platelet adhesion and aggregation under elevated shear stress. *Blood* 108(6):1903–1910.
10. Savage B, Saldívar E, Ruggeri ZM (1996) Initiation of platelet adhesion by arrest onto fibrinogen or translocation on von Willebrand factor. *Cell* 84(2):289–297.
11. Sadler JE (1998) Biochemistry and genetics of von Willebrand factor. *Annu Rev Biochem* 67:395–424.
12. Savage B, Sixma JJ, Ruggeri ZM (2002) Functional self-association of von Willebrand factor during platelet adhesion under flow. *Proc Natl Acad Sci USA* 99(1):425–430.
13. De Gennes PG (1974) Coil-stretch transition of dilute flexible polymers under ultra-high velocity gradients. *J Chem Phys* 60(12):5030–5042.
14. Springer TA (2014) von Willebrand factor, Jedi knight of the bloodstream. *Blood* 124(9):1412–1425.
15. Sing CE, Alexander-Katz A (2010) Elongational flow induces the unfolding of von Willebrand factor at physiological flow rates. *Biophys J* 98(9):L35–L37.
16. Zhang X, Halvorsen K, Zhang CZ, Wong WP, Springer TA (2009) Mechanoenzymatic cleavage of the ultralarge vascular protein von Willebrand factor. *Science* 324(5932): 1330–1334.
17. Sadler JE (2005) New concepts in von Willebrand disease. *Annu Rev Med* 56:173–191.
18. Ruggeri ZM, Mendolicchio GL (2007) Adhesion mechanisms in platelet function. *Circ Res* 100(12):1673–1685.
19. Emsley J, Cruz M, Handin R, Liddington R (1998) Crystal structure of the von Willebrand Factor A1 domain and implications for the binding of platelet glycoprotein Ib. *J Biol Chem* 273(17):10396–10401.
20. Huizinga EG, et al. (2002) Structures of glycoprotein Ibα and its complex with von Willebrand factor A1 domain. *Science* 297(5584):1176–1179.
21. Blenner MA, Dong X, Springer TA (2014) Structural basis of regulation of von Willebrand factor binding to glycoprotein Ib. *J Biol Chem* 289(9):5565–5579.
22. Othman M (2011) Platelet-type Von Willebrand disease: Three decades in the life of a rare bleeding disorder. *Blood Rev* 25(4):147–153.
23. Dumas JJ, et al. (2004) Crystal structure of the wild-type von Willebrand factor A1-glycoprotein Ibα complex reveals conformation differences with a complex bearing von Willebrand disease mutations. *J Biol Chem* 279(22):23327–23334.
24. Bustamante C, Smith SB, Liphardt J, Smith D (2000) Single-molecule studies of DNA mechanics. *Curr Opin Struct Biol* 10(3):279–285.
25. Dudko OK, Hummer G, Szabo A (2008) Theory, analysis, and interpretation of single-molecule force spectroscopy experiments. *Proc Natl Acad Sci USA* 105(41):15755–15760.
26. Pierse CA, Dudko OK (2013) Kinetics and energetics of biomolecular folding and binding. *Biophys J* 105(9):L19–L22.
27. Kim YC, Tang C, Clore GM, Hummer G (2008) Replica exchange simulations of transient encounter complexes in protein−protein association. *Proc Natl Acad Sci USA* 105(35):12855–12860.
28. Camacho CJ, Weng Z, Vajda S, DeLisi C (1999) Free energy landscapes of encounter complexes in protein-protein association. *Biophys J* 76(3):1166–1178.
29. Miura S, et al. (2000) Interaction of von Willebrand factor domain A1 with platelet glycoprotein Ibα-(1–289). Slow intrinsic binding kinetics mediate rapid platelet adhesion. *J Biol Chem* 275(11):7539–7546.
30. Ju L, Dong JF, Cruz MA, Zhu C (2013) The N-terminal flanking region of the A1 domain regulates the force-dependent binding of von Willebrand factor to platelet glycoprotein Ibα. *J Biol Chem* 288(45):32289–32301.
31. Chen J, et al. (2014) Exploiting the kinetic interplay between GPIbα–VWF binding interfaces to regulate hemostasis and thrombosis. *Blood* 124(25):3799–3807.
32. Lan HY (2003) Tubular epithelial-myofibroblast transdifferentiation mechanisms in proximal tubule cells. *Curr Opin Nephrol Hypertens* 12(1):25–29.
33. Luo SZ, et al. (2007) Glycoprotein Ibα forms disulfide bonds with 2 glycoprotein Ibβ subunits in the resting platelet. *Blood* 109(2):603–609.
34. Nesbitt WS, et al. (2009) A shear gradient-dependent platelet aggregation mechanism drives thrombus formation. *Nat Med* 15(6):665–673.
35. Zhang Y, Dudko OK (2013) A transformation for the mechanical fingerprints of complex biomolecular interactions. *Proc Natl Acad Sci USA* 110(41):16432–16437.
36. Hampshire DJ, Goodeve AC (2011) The International Society on Thrombosis and Haematosis von Willebrand Disease Database: An update. *Semin Thromb Hemost* 37(5):470–479.
37. Othman M, Kaur H, Emsley J (2013) Platelet-type von Willebrand disease: New insights into the molecular pathophysiology of a unique platelet defect. *Semin Thromb Hemost* 39(6):663–673.

Supporting Information

Kim et al. 10.1073/pnas.1501689112

SI Materials and Methods

Off-Rate Constant Estimations. The lifetime of a bond at a constant force can be calculated from histograms of the unbinding forces in force rip experiments as described previously (1, 2). Briefly, the k_{off} of a bond as a function of the force can be given as

$$k_{\text{off}}(F)=\frac{\dot{F}*p(\text{rupture at }F)}{P(\text{rupture above }F)} \qquad \textbf{[S1]}$$

where P stands for probability of unbinding above a given force, p is probability of unbinding at a given force, and $\dot{F}$ is the force loading rate. The probabilities of rupturing above and at a given force in Eq. **S1**, can be calculated from unbinding histograms using

$$k_{\text{off}}(F_k)=\frac{h_k\dot{F}\left(F_o+\left(k-\frac{1}{2}\right)\Delta F\right)}{\left(h_k/2+\sum_{i=k+1}^{N}h_i\right)\Delta F} \qquad \textbf{[S2]}$$

where ΔF is the bin width of the rupture force histogram that starts at F_o, h_i is the fraction of ruptures in the ith bin normalized by the total count, and i and k are bin numbers. Plots of $k(F)$ vs. F were fit with a Bell equation using linear least squares methods (3, 4)

$$k_{\text{off}}(F)=k_{\text{off}}^{0}\exp\left(\frac{\sigma F}{k_BT}\right) \qquad \textbf{[S3]}$$

where k_{off}^{0} is the zero force unbinding rate and σ is the distance in an energy landscape from the bound state to the maximum height of the energy barrier for unbinding (Fig. 2 *J–L*). From Eq. **S3**, a probability distribution for unbinding as a function of force can be obtained,

$$p(F)=\frac{k_{\text{off}}(F)*\exp\left(-\int_0^F k_{\text{off}}(f)\dot{F}(f)^{-1}df\right)}{\dot{F}(F)} \qquad \textbf{[S4]}$$

The kinetic values from fitting using Eq. **S3** were used to calculate the probability distributions for dissociation pathways 1 and 2, which are shown as curves in Fig. 2 *A–I* (1). For events in middle bins, between the peaks for states 1 and 2, events were apportioned into states 1 and 2 according to iterative fits.

On-Rate Constant Estimations. Binding histograms as a function of force can be converted into binding kinetics at constant force using an equation from Pierse and Dudko to account for rebinding data (5),

$$k_{\text{on}}(F)=\frac{\dot{F}*P(\text{binding at }F)}{P(\text{binding below }F)} \qquad \textbf{[S5]}$$

$$k_{\text{on}}(F_k)=\frac{h_k\dot{F}\left(F_o+\left(k-\frac{1}{2}\right)\Delta F\right)}{\left(h_k/2+\sum_{i=1}^{N}h_i\right)\Delta F} \qquad \textbf{[S6]}$$

Rebinding is a function of the energy barrier to rebinding, the distance to the energy barrier from the unbound state, and the attempt frequency for hopping over the barrier (related to k_{on}^{0}). In bulk phase, the attempt frequency is directly proportional to the concentration of ligands in solution. In the case of our ReaLiSM construct stretched by a laser tweezers, the attempt frequency is governed by the stiffness of the trap, the DNA handles, and the linker between the receptor and ligand. In this case, the probability of binding at a given force can be derived to be (5)

$$p(F)=\frac{k_{\text{on}}(F)}{|\dot{F}(F)|}\exp\left[-\frac{k_BT*k_{\text{on}}(F)}{|\dot{F}(F)|*\sigma_{\text{on}}^{RTL}}\left[1+\frac{\kappa_s}{\kappa_u(F)}\right]^{\frac{\nu}{\nu-1}}\left[1+\frac{\nu F\sigma_{on}^{RTL}}{\Delta G_{on}^{RTL}}\right]^{1-\frac{1}{\nu}}\right] \qquad \textbf{[S7]}$$

where

$$k_{\text{on}}(F)=k_{\text{on}}^{0\,RTL}\left[1+\frac{\kappa_s}{\kappa_u(F)}\right]^{\frac{1}{\nu}-\frac{1}{2}}\left[1+\frac{\nu F\sigma_{\text{on}}^{RTL}}{\Delta G_{\text{on}}^{RTL}}\right]^{\frac{1}{\nu}-1} * \exp\left\{\frac{\Delta G_{\text{on}}^{RTL}}{k_BT}*\left[1-\left[1+\frac{\kappa_s}{\kappa_u(F)}\right]^{\frac{2\nu}{1-\nu}-1}\left[1+\frac{\nu F\sigma_{\text{on}}^{RTL}}{\Delta G_{\text{on}}^{RTL}}\right]^{\frac{1}{\nu}}\right]\right\}. \qquad \textbf{[S8]}$$

Here $\Delta G_{\text{on}}^{\text{RTL}}$ is the energy barrier to rebinding, σ_{on}^{RTL} is the distance from the unbound energy well to the binding energy barrier, κ_s is the spring constant of the pulling device (the trap and DNA handles in series; 0.05 pN/nm is the measured value for our laser tweezers setup), κ_u is the spring constant of the unbound receptor−tether−ligand (RTL) interaction, and ν is a scaling factor that depends on the shape of the energy barrier (typically a value between 0.5 and 0.66). Note that the units of $p(F)$ are in units of 1/force; therefore, to use Eq. **S7** for fitting, histograms must be normalized and divided by the histogram bin width, to get the histogram data in units of 1/force.

Fitting using Eqs. **S7** and **S8** applied to the $p(F)$ values was performed by minimizing the sum of squared errors between the difference of $p(F)$ and the normalized histogram data using the fminsearch tool in MATLAB. Fminsearch was iteratively run using a series of values for ν (0.5–0.66), and initial values for k_{on}^{0} (1–200 s^{-1}), ΔG_{on} (1–100 k_BT), and σ_{on} (0.7–100 nm). Before fitting, binding events in the overlap region between state 1 and state 2 peaks were partitioned into state 1 or state 2. This partitioning and fitting process was iterated until the lowest mean squared error was achieved. Best fits were typically found with $\nu = 0.5$ or 0.53; fits fixed at the two ν values yield similar k_{on}^{0} (5–15% variation), σ_{on} values (3–6%), and ΔG_{on} values (20–35%). Values reported in the main text Fig. 3 and Tables S2 and S3 represent $\nu = 0.5$. During fitting, a constraint was applied, such that $k_{\text{on}}^{0} > k_{\text{on}}(F)$.

The parameters giving the smallest weighted sum of squared errors (WSSE) were chosen as the best-fit parameters: $\text{WSSE}=\sum_{i=1}^{n}(h_i-p_i)^2$, where n is the number of histogram bins, h_i is the normalized event frequency in the histogram bin, and p_i is the probability function at force i, corresponding to bin i. Error values reported for k_{on}^{0}, ΔG, and σ represent 1 SD or a 68% confidence interval. Confidence intervals were determined through the following process: First, the WSSE was calculated as a function of fitting parameter value. The WSSE can then be exponentiated and normalized to determine a probability distribution function ($\text{PDF}(\gamma_i)=\frac{1}{C}e^{-\text{WSSE}_{\gamma_i}}$, where $\text{PDF}(\gamma_i)$ is the probability of finding parameter (γ) with value "i" and c is a normalizing constant, which is equal to $\sum e^{-\text{WSSE}_{\gamma_i}}$). The 68% confidence intervals were then calculated as the parameter space for which 15.8% < PDF <

84.2%. For ΔG_{on} and k^0_{on}, the PDF is asymmetric with respect to the best-fit parameter value; however, for simplicity, we assume a Gaussian distribution of the PDF for all three variables.

Decoupling the Effects of the Tether from the Intrinsic Binding Kinetics. The on-rate (k^0_{on}), energy barrier height (ΔG_{on}), and exponential factor (σ_{on}) found using Eqs. **S7** and **S8** apply to the RTL construct but do not represent the intrinsic binding kinetics of the receptor and ligand in the absence of the tether. To obtain the intrinsic receptor−ligand (RL) binding kinetics, one must account for the effects of the tether. This can be done using a transformation (5),

$$\alpha = \frac{2\left(\Delta G^{\mathrm{RTL}}_{\mathrm{on}} - G_{\mathrm{teth}}(\Delta l) + G_{\mathrm{teth}}\left(\Delta l + \sigma^{\mathrm{RTL}}_{\mathrm{on}}\right)\right)}{\sigma^{\mathrm{RTL}}_{\mathrm{on}} F_{\mathrm{teth}}\left(\Delta l + \sigma^{\mathrm{RTL}}_{\mathrm{on}}\right)} \qquad \textbf{[S9]}$$

$$\sigma^{\mathrm{RL}}_{\mathrm{on}} = \sigma^{\mathrm{RTL}}_{\mathrm{on}}\left(\frac{\alpha-1}{\alpha-2}\right) \qquad \textbf{[S10]}$$

$$\Delta G^{\mathrm{RL}}_{\mathrm{on}} = \frac{(\alpha-1)^2}{2(\alpha-2)}\sigma^{\mathrm{RTL}}_{\mathrm{on}} F_{\mathrm{teth}}\left(\Delta l + \sigma^{\mathrm{RTL}}_{\mathrm{on}}\right) \qquad \textbf{[S11]}$$

$$k^{0\ \mathrm{RL}}_{\mathrm{on}} = k^{0\ \mathrm{RTL}}_{\mathrm{on}} \frac{\left(\beta \Delta G^{\mathrm{RL}}_{\mathrm{on}}\right)^{3/2}}{\left(\beta \Delta G^{\mathrm{RTL}}_{\mathrm{on}}\right)^{\frac{1}{\nu}-0.5}} \left[\frac{\sigma^{\mathrm{RTL}}_{\mathrm{on}}}{\sigma^{\mathrm{RL}}_{\mathrm{on}}}\right]^2 \exp\left[\beta\left(\Delta G^{\mathrm{RTL}}_{\mathrm{on}} - \Delta G^{\mathrm{RL}}_{\mathrm{on}}\right)\right] \qquad \textbf{[S12]}$$

where α is the transformation factor, β is the inverse of k_BT (the Boltzmann factor), G_{teth} and F_{teth} are the potential and force extension relationship of the tether defined by the WLC model (see Fig. 1 for WLC fitting parameters), $\sigma^{\mathrm{RTL}}_{\mathrm{on}}$, $\Delta G^{\mathrm{RTL}}_{\mathrm{on}}$, and $k^{0\ \mathrm{RTL}}_{\mathrm{on}}$ are the fitting parameters for the RTL construct found from fitting using Eqs. **S7** and **S8**, and $\sigma^{\mathrm{RL}}_{\mathrm{on}}$, $\Delta G^{\mathrm{RL}}_{\mathrm{on}}$, and $k^{0\ \mathrm{RL}}_{\mathrm{on}}$, are the intrinsic RL parameters. The parameter Δl describes the extension of the tether in the direction of the pulling force, when the ligand reaches the transition state before binding.

Determining Δ*l*. Δl can be calculated from the distance from the bound state to the transition state, i.e., the σ value derived from unbinding experiments in Fig. 2, combined with geometrical corrections accounting for the location of the ligand within the binding pocket of the receptor,

$$\Delta l = \sigma_{\mathrm{off}} + a - \Delta a_{\mathrm{rec}} - \Delta a_{\mathrm{lig}}, \qquad \textbf{[S13]}$$

where a is the distance between tether attachment points along the pulling coordinate of the bound RTL construct and Δa_{rec} and Δa_{lig} are correction factors accounting for the rotation of the position of the tether attachment point in the bound versus unbound state along the pulling coordinate (5) (Figs. S1 and S2). Estimating a and Δa terms can be done using trigonometry and coordinates from crystal structures of the bound receptor and ligand. When force is applied, the pulling coordinate will be defined by the closest residue to the pulling force at each termini of the RL complex that is stably integrated into the structure (for example, with backbone hydrogen bonds, disulfide bonds, or significant sidechain hydrophobic burial). A large number of crystal structures and independent examples in crystal lattices of the A1-GPIbα complex and isolated A1 and GPIbα are available (see ref. 6 for a list). Conservation of position in independent structures was another criterion for residues that were chosen as tether attachment points. We used the A1-GPIbα crystal structure (protein databank identification 4C2A) (6) both because it is the highest resolution available and its A1-GPIbα orientation is similar to that of multiple other complex structures (6).

We defined the pulling coordinate as the line connecting the Cα of A1 Tyr-1271 to the Cα of GPIbα Cys-264. The tether attachment points were taken as A1 Glu-1463 and GPIbα Ile-3. The distance between these two residues is 3.0 nm, which corresponds to a distance of 0.7 nm when projected onto the pulling coordinate axis (Fig. S1*A*); therefore, 0.7 nm serves as the value for a for state 1. To estimate Δa_{rec}, we must consider the orientation of the receptor after the ligand has unbound. In this case, we estimate a new pulling coordinate for the unbound state of GPIbα between its residues Ile-3 and Cys-264. The distance between these residues of 6.7 nm (R2 in Fig. S1 *A* and *B*) projects onto the bound state pulling coordinate a distance of 5.9 nm (R1 in Fig. S1*A*). Therefore, $\Delta a_{\mathrm{rec}} = 6.7$ nm − 5.9 nm = 0.8 nm. Δa_{lig} is calculated by projecting the distance between A1 Glu-1463 and Tyr-1271 onto the bound state pulling coordinate, which gives $L_1 = 0.1$ nm (Fig. S1*A*). In the unbound state, under force, Glu-1463 and Tyr-1271 will rotate and align with the pulling coordinate, giving a distance in the unbound state of $L_2 = 1.2$ nm (Fig. S1*B*); therefore, $\Delta a_{\mathrm{lig}} = 1.2$ nm − 0.1 nm = 1.1 nm. Including all terms, $\Delta l = \sigma_{\mathrm{off}} + 0.7$ nm − 0.8 nm − 1.1 nm = $\sigma_{\mathrm{off}} - 1.2$ nm (σ_{off} is determined in Fig. 2 and ranges from 1.7 nm to 2.5 nm for state 1 and 1.1–1.6 nm for state 2).

All RL values reported here assume that states 1 and 2 have the a, Δa_{rec}, and Δa_{lig} geometric values described above. However, we wondered how sensitive the reported RL values of σ, k_{on}, and ΔG would be to changes in the geometric estimates. For example, an important caveat is that Δl could differ for states 1 and 2. Therefore, we examined the consequence for estimates of Δl if state 2 corresponded to a conformation of A1 in which all residues on either side of the long-range disulfide bond unfolded and became extended. In this case, we define the pulling coordinate axis as between A1 Cys-1272 and GPIbα Cys-264, and the tether attachment point on A1 becomes residue Cys1458 (Fig. S2). Using the same trigonometric considerations, we find an a value of 0.7 nm, a Δa_{rec} value of 0.7 nm ($R_2 = 6.7$ nm, $R_1 = 6.0$ nm), and a Δa_{lig} value of [0.64 nm (L_2) − 0.62 nm (L_1)] = 0.02 nm. Therefore, $\Delta l = \sigma_{\mathrm{off}} + 0.7\text{–}0.7\text{–}0$ nm = σ_{off}. We find that if we use $\Delta l = \sigma$ instead of $\Delta l = \sigma$ -1.2 nm, the reported RL values for wild-type, the two mutant constructs, and states 1 and 2 change from −22 to 0% for k_{on}, from 10% to 25% for σ_{on}, and from 20% to 45% for ΔG. These changes are comparable to our experimental errors, showing that our results are relatively insensitive to uncertainties in the geometric correction factors for the transition state.

Tables S1 and S2 show k^0_{on}, σ_{on}, and ΔG values for the 43- and 26-residue linker constructs, respectively. The RTL values for states 1 and 2 of wild-type and mutant ReaLiSM constructs are derived from the fits shown in Fig. 3. The RL values are calculated as described above, using WLC parameters from Fig. 1*C* and $\Delta l = \sigma_{\mathrm{off}} - 1.2$ nm.

Conversion to Solution On-Rates and K_D. Solution on-rates ($\mathrm{M}^{-1}\mathrm{s}^{-1}$) are defined as the product of the ligand concentration in an encounter complex and the intrinsic RL on-rate in units of s^{-1} (3). To estimate the effective concentration of ligand, the crystal structure 4C2A was used to determine that the distance, d, between the center of masses of A1 and GPIbα in the bound state (6) is 2.8 nm. As described in the main text *Discussion* and Fig. 4*F*, our physical model of the encounter complex has radius $r = d + \sigma_{\mathrm{off}} + \sigma_{\mathrm{on}}$. The effective concentration, C, of one reactant with respect to the other is computed as one molecule divided by Avogadro's number and the volume of a sphere with radius r, i.e., $4/3\pi r^3$. We find effective concentrations ranging from 1 mM to 4 mM using this estimate, in reasonable agreement with effective concentrations calculated for other tethered RL pairs (7).

To calculate the effective concentration under force, we use the average end-to-end length of the tether, t. At high forces, the average length of the tether under external force (F_{ext}) is given by (8)

$$\langle t \rangle = L_c\left[1 - 0.5\sqrt{k_B T / F_{\text{ext}} L_p}\right] \qquad \textbf{[S14]}$$

where L_p and L_c are the persistence and contour lengths of a worm-like chain polymer.

In the case considered in the main text *Discussion* and Fig. 4 of a 15-pN external force, F_{ext} in Eq. **S14** is set equal to 15 pN. At 15 pN, $<t>$ equals 10.4 nm and 7.1 nm for the 43- and 26-residue linkers, respectively. Under external force, we define r as $d + <t>$, yielding effective concentrations of 130 μM and 310 μM for the 43- and 26-residue linkers.

1. Kim J, Zhang CZ, Zhang X, Springer TA (2010) A mechanically stabilized receptor-ligand flex-bond important in the vasculature. *Nature* 466(7309):992–995.
2. Dudko OK, Hummer G, Szabo A (2008) Theory, analysis, and interpretation of single-molecule force spectroscopy experiments. *Proc Natl Acad Sci USA* 105(41):15755–15760.
3. Bell GI (1978) Models for the specific adhesion of cells to cells. *Science* 200(4342): 618–627.
4. Evans EA, Calderwood DA (2007) Forces and bond dynamics in cell adhesion. *Science* 316(5828):1148–1153.
5. Pierse CA, Dudko OK (2013) Kinetics and energetics of biomolecular folding and binding. *Biophys J* 105(9):L19–L22.
6. Blenner MA, Dong X, Springer TA (2014) Structural basis of regulation of von Willebrand factor binding to glycoprotein Ib. *J Biol Chem* 289(9):5565–5579.
7. Krishnamurthy VM, Semetey V, Bracher PJ, Shen N, Whitesides GM (2007) Dependence of effective molarity on linker length for an intramolecular protein-ligand system. *J Am Chem Soc* 129(5):1312–1320.
8. Marko JF, Siggia ED (1995) Stretching DNA. *Macromolecules* 28(26):8759–8770.

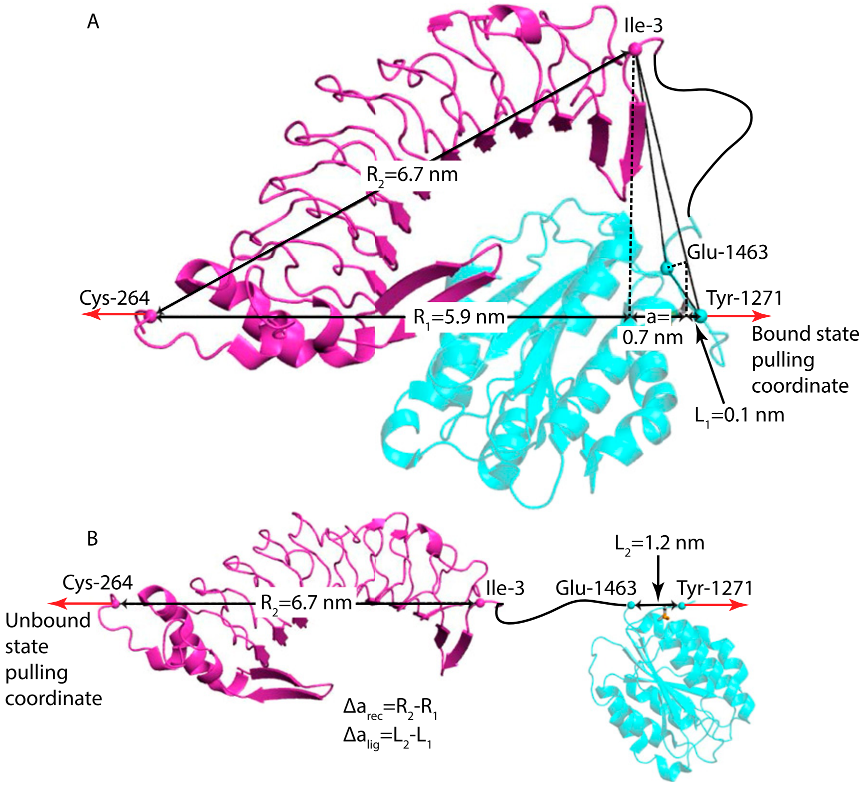

Fig. S1. Finding geometric values required for converting RTL to RL parameters. (*A*) Crystal structure showing the bound state of A1-GPIbα, defining the pulling coordinate. The value for *a* is found by projecting the Glu-1463-Ile-3 vector onto the plane defined by Ile-3, Tyr-1271, and Cys-264; *a* = 0.7 nm. (*B*) Crystal structures of A1 and GPIbα in the unbound state, oriented along the unbound state pulling coordinate. Arrow-headed lines in *A* and *B* represent the orientation and distance between the receptor−tether attachment points and their projections (dashed lines) onto the pulling coordinates in the bound (R_1 and L_1) and unbound (R_2 and L_2) states. Δa_{rec} is defined as the difference in the receptor tether attachments point (Ile-3) between the bound R_1 and unbound R_2 states. Δa_{lig} is defined as the difference in the ligand tether attachment point (Glu-1463) projected onto the pulling coordinate axis between the bound (L_1) and unbound states (L_2).

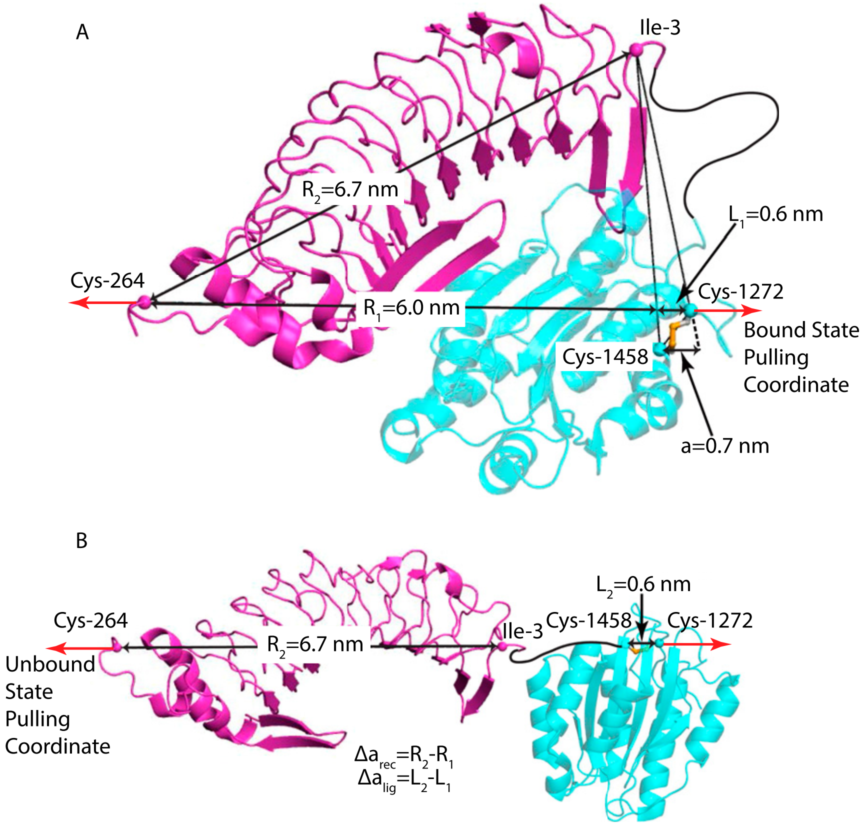

Fig. S2. Hypothetical test of how much geometric parameters would change if there was a conformational change in A1 in state 2. *A* and *B* are the same as in Fig. S1, but assuming that the hydrogen bonds in the N- and C-terminal regions of A1 external to the long-range disulfide bond would all be broken in a high-affinity state 2. Breaking of the hydrogen bonds moves the tether attachment points in A1 directly to A1 Cys-1272 and A1 Cys-1458.

Table S1. Lack of history dependence of binding and unbinding events (40 nm/s)

		43-Residue tether		26-Residue tether	
	Event type	Measured events	Events if no hysteresis	Measured events	Events if no hysteresis
	Unbinding-binding				
Wild-type	state1-state1	39	37	14	10
Wild-type	state1-state2	38	40	9	13
Wild-type	state2-state1	23	25	7	11
Wild-type	state2-state2	29	27	19	15
M239V	state1-state1	85	75	32	30
M239V	state1-state2	5	15	3	5
M239V	state2-state1	26	36	11	13
M239V	state2-state2	18	8	4	2
R1306Q	state1-state1	58	53	24	14
R1306Q	state1-state2	18	23	14	24
R1306Q	state2-state1	37	42	15	25
R1306Q	state2-state2	22	17	56	46
	Binding-unbinding				
Wild-type	state1-state1	34	30	7	6
Wild-type	state1-state2	16	20	5	6
Wild-type	state2-state1	33	37	8	9
Wild-type	state2-state2	27	23	12	11
M239V	state1-state1	77	69	30	29
M239V	state1-state2	20	28	11	12
M239V	state2-state1	6	14	3	4
M239V	state2-state2	14	6	3	2
R1306Q	state1-state1	46	46	23	13
R1306Q	state1-state2	36	36	13	23
R1306Q	state2-state1	20	20	13	23
R1306Q	state2-state2	16	16	51	41

If there is no hysteresis, the frequency of two types of events happening in succession is the product of the overall frequencies of the two events. These frequencies, times the total number of events, are used to calculate "events if no hysteresis."

Table S2. Force-dependent A1-GPIbα binding constants measured with a 43-residue linker (RTL) and calculated without the linker (RL)

	$k_{\mathrm{on}}^{0\ \mathrm{RTL}}$, s^{-1}	$k_{\mathrm{on}}^{0\ \mathrm{RL}}$, s^{-1}	$k_{\mathrm{on}}^{0\ \mathrm{RL}}$, $\times 10^{3}$ M$^{-1}\cdot$s^{-1}	$\sigma_{\mathrm{on}}^{\mathrm{RTL}}$, nm	$\sigma_{\mathrm{on}}^{\mathrm{RL}}$, nm	ΔG^{RTL}, k_BT	ΔG^{RL}, k_BT
WT state 1	5.8 ± 2.5	1.7 ± 1.1	1.9 ± 1.2	1.58 ± 0.10	2.3 ± 0.5	1.5 ± 0.3	2.5 ± 0.8
WT state 2	52 ± 16	18 ± 9	9.9 ± 5.0	1.31 ± 0.05	1.6 ± 0.3	1.5 ± 0.2	1.9 ± 0.5
M239V state 1	16 ± 5	5.4 ± 2.7	3.1 ± 1.6	1.15 ± 0.03	1.4 ± 0.2	1.5 ± 0.2	1.9 ± 0.5
M239V state 2	180 ± 50	65 ± 30	27 ± 13	0.97 ± 0.04	1.1 ± 0.2	1.5 ± 0.2	1.7 ± 0.4
R1306Q state 1	5.9 ± 2.6	2.3 ± 1.3	1.2 ± 0.7	1.18 ± 0.06	1.4 ± 0.3	1.6 ± 0.4	1.9 ± 0.5
R1306Q state 2	110 ± 30	39 ± 18	13 ± 6	1.10 ± 0.04	1.2 ± 0.2	1.5 ± 0.2	1.6 ± 0.4

RTL binding constants were converted into RL values using Eqs. **S9**–**S13**.

Table S3. Force-dependent A1-GPIbα binding constants measured with a 26-residue linker (RTL) and calculated without the linker (RL)

	$k_{\mathrm{on}}^{0\ \mathrm{RTL}}$, s^{-1}	$k_{\mathrm{on}}^{0\ \mathrm{RL}}$, s^{-1}	$k_{\mathrm{on}}^{0\ \mathrm{RL}}$, $\times 10^{3}$ M$^{-1}\cdot$s^{-1}	$\sigma_{\mathrm{on}}^{\mathrm{RTL}}$, nm	$\sigma_{\mathrm{on}}^{\mathrm{RL}}$, nm	ΔG^{RTL}, k_BT	ΔG^{RL}, k_BT
WT state 1	20 ± 9	5.0 ± 3.6	6.5 ± 4.7	1.51 ± 0.14	2.7 ± 0.8	1.5 ± 0.4	3.2 ± 1.2
WT state 2	210 ± 50	61 ± 30	41 ± 20	1.41 ± 0.06	2.0 ± 0.4	1.5 ± 0.2	2.2 ± 0.6
M239V state 1	7.1 ± 3.7	2.4 ± 1.7	1.4 ± 1.0	1.09 ± 0.12	1.4 ± 0.4	1.5 ± 0.5	2.0 ± 0.7
M239V state 2	65 ± 30	23 ± 15	9.1 ± 5.9	0.87 ± 0.06	1.0 ± 0.2	1.5 ± 0.6	1.8 ± 0.5
R1306Q state 1	12 ± 6	3.9 ± 2.7	2.2 ± 1.5	1.22 ± 0.16	1.6 ± 0.5	1.5 ± 0.5	2.0 ± 0.8
R1306Q state 2*	200 ± 50	68 ± 29	20 ± 8	0.94 ± 0.03	1.0 ± 0.2	1.5 ± 0.2	1.7 ± 0.4

RTL binding constants were converted into RL values using Eqs. **S9**–**S13**.

*RL values for R1306Q state 2 were calculated using $\Delta l = 0$, because $\sigma_{\mathrm{off}} = 1.06$ nm, so 1.06–1.2 nm would give a negative value for Δl.

Table S4. VWD 2B and PT-VWD mutations increase affinity relative to wild-type much more in presence than absence of force

		k_{on}^{RL}, s^{-1}	k_{off}, s^{-1}	k_{on}^{MUT} increase	k_{off}^{MUT} decrease	K_{D}^{MUT} decrease	$k_{2\ on}/k_{1\ on}$ increase
M239V	state 1 (0 pN)	3.9 ± 1.6	0.0029 ± 0.0007	1.2	1.6	2.0	
	state 2 (0 pN)	44 ± 17	0.0005 ± 0.0003				11
M239V	state 1 (15 pN)	0.026 ± 0.016	3.2 ± 1.5				
	state 2 (15 pN)	1.2 ± 0.5	0.16 ± 0.13	39	5.1	230	50
R1306Q	state 1 (0 pN)	3.1 ± 1.5	0.0055 ± 0.0015	0.9	0.9	1.0	
	state 2 (0 pN)	54 ± 17	0.0018 ± 0.0006				17
R1306Q	state 1 (15 pN)	0.01 ± 0.01	2.34 ± 1.13				
	state 2 (15 pN)	1.1 ± 0.4	0.086 ± 0.034	36	9.4	260	100
WT	state 1 (0 pN)	3.4 ± 1.9	0.0047 ± 0.0015	1	1	1	
	state 2 (0 pN)	40 ± 16	0.0022 ± 0.0007				12
WT	state 1 (15 pN)	0.001 ± 0.001	46 ± 32				
	state 2 (15 pN)	0.03 ± 0.02	0.81 ± 0.39	1	1	1	40

The $k_{on}^{0\ RL}$ values and k_{off}^{0} values are shown for mutant and WT at zero force in state 1, which predominates at low force. We also show values for state 2, to allow comparison in the main text discussion of how much switching to state 2 increases on-rate. At 15 pN, state 2 predominates, and k_{on}^{RL} and k_{off} are calculated at 15 pN in state 2. The k_{on}^{MUT} increase is defined as: $k_{on}^{RL\ MUT}/k_{on}^{RL\ WT}$; k_{off}^{MUT} decrease is defined as: $k_{off}^{WT}/k_{off}^{MUT}$. The solution phase dissociation constant K_{D}^{MUT} decrease is defined as K_{D}^{WT}/K_{D}^{MUT}. The $k_{2\ on}/k_{1\ on}$ increase represents the on-rate enhancement achieved by switching from state 1 to state 2. The k_{on}^{RL} values are averages of results for 43- and 26-residue linkers.